PHYSICAL REVIEW B **88**, 174416 (2013)

Phase relations, crystal chemistry, and physical properties of $MgZn_2$-type Laves phases in the Mn-Cu-Si and Mn-Ni-Si systems

X. Yan,[1,2,*] M. W. Pieper,[3] H. Michor,[1] G. Hilscher,[1] M. Reissner,[1] A. Grytsiv,[2] P. Rogl,[2,†] V. Pomjakushin,[4] G. Giester,[5]
E. Bauer,[1] and S. Paschen[1]

[1]*Institute of Solid State Physics, Vienna University of Technology, Wiedner Hauptstr. 8-10, 1040 Vienna, Austria*
[2]*Institute of Physical Chemistry, University of Vienna, Währingerstr. 42, 1090 Vienna, Austria*
[3]*Institute of Experimental Physics, Karl-Franzens University, Universitätsplatz 5, A-8010 Graz, Austria*
[4]*Laboratorium für Neutronenstreuung, ETHZ & PSI, Villigen, Switzerland*
[5]*Institute of Mineralogy and Crystallography, University of Vienna, Althanstrasse 14, A-1090 Wien, Austria*

(Received 16 September 2013; published 19 November 2013)

In this study, we present the phase relations, crystal structure, and physical properties of the $MgZn_2$-type Laves phases in the Mn-Cu-Si and Mn-Ni-Si systems. Our results evidence that the homogeneous regime of the Laves phase in the Mn-Cu-Si system at 800 °C ranges from 32.5 to 36.7 at.% Mn and from 11.5 to 13.5 at.% Si, indicating the Laves phase in this system having an ideal stoichiometry AB_2, inconsistent with previous reports. For structural and physical property investigations, two alloys with compositions $MnCu_{1.65}Si_{0.35}$ and $MnNi_{1.25}Si_{0.75}$ are considered. In both alloys, Mn atoms are preferably situated at the $4f$ site and Cu(Ni) and Si share the $2a$ and $6h$ sites. Both are antiferromagnets with $T_N \approx 800$ K for $MnCu_{1.65}Si_{0.35}$ and $T_N \approx 630$ K for $MnNi_{1.25}Si_{0.75}$. Rietveld refinements of the room-temperature neutron diffraction data demonstrate that in both cases only the Mn atoms carry magnetic moments, which are aligned antiferromagnetically along the c axis. The magnetic moments at room temperature are $2.7\mu_B$/Mn for $MnCu_{1.65}Si_{0.35}$ and $2.9\mu_B$/Mn for $MnNi_{1.25}Si_{0.75}$, respectively. The magnetic properties are confirmed by transport, magnetization, NMR measurements, and band-structure calculations.

DOI: 10.1103/PhysRevB.88.174416 PACS number(s): 81.30.−t, 75.50.Ee, 75.30.Kz, 31.15.A−

I. INTRODUCTION

Interest in the Mn-Cu-Si system was triggered initially by the fascinating mechanical properties, e.g., combining good strength and hardness with reasonable malleability of the Cu rich alloys.[1–5] Several isothermal sections in the Cu rich corner at different temperatures were established experimentally, although discrepancies were observed. A few reviews on this system were presented in the literature.[6–8] Interest in the Mn rich corner started in 1973, when Mukherjee and Gupta reported[9] that a Laves phase with $MgZn_2$-type has an odd stoichiometry around a mean composition of $Mn_{50.2}Cu_{32.5}Si_{17.3}$, which is unexpected with respect to the general Laves stoichiometry AB_2. Later on the same authors[10] located this phase in the 700 °C isothermal section on the basis of light optical microscopy (LOM) and x-ray powder diffraction (XPD) analysis, which indicated that the phase is in equilibrium with Mn_5Si_3, Mn_3Si, γ phase, and has a limited homogeneity range. Model calculations of x-ray powder intensities were not perfect but showed acceptable agreement for Mn atoms at the CN16 ($4f$) sites with the remaining Mn, Cu, and Si atoms sharing the CN12 ($2a$ and $6h$) sites.[10] Thermodynamic calculations questioned the phase relations associated with the Laves phase, but *not* the location of the Laves phase in the isothermal section.[11] An unusual stoichiometry has also been reported for the Laves phase in the Mn-Ni-Si system[9,12,13] with a rather large homogeneity range at 800 °C extending from 33 to 39 at.% Mn and from 22 to 30 at.% Cu.[13,14] However, no specific information on atom occupation and atomic coordinates was provided. Compounds of Mn-T-X (T = transition metal element and X = 4B element), crystallizing in different structure types, exhibit a variety of types of magnetic ordering.[15–17] In the Mn-Ni-Si system, cubic Mn_3Ni_2Si (space group: $Fd\bar{3}m$) has been demonstrated to be an antiferromagnet with $T_N = 215$ K possessing a magnetic moment of $0.57(5)\mu_B$ at 78 K localized on manganese ions.[18] Investigation of another cubic phase $Mn_6Ni_{16}Si_7$ [$Mn_6Cu_{16}Si_7$-type phase (G phase), space group: $Fm\bar{3}m$] showed antiferromagetism below 205 K and a magnetic moment of $2.7\mu_B$ for manganese ions.[19] No magnetic property information is available for the Laves phase in both systems Mn-Ni-Si and Mn-Cu-Si albeit the Laves phases generally exhibit very interesting magnetic features. Therefore the present work aims to provide detailed information on the crystal structure, magnetic properties, and phase relations concerning the $MgZn_2$-type Laves phases in both systems Mn-Cu-Si and Mn-Ni-Si.

II. EXPERIMENTAL

A. Sample preparation and characterization

We firstly tried to prepare one alloy with a nominal composition $Mn_{50.2}Cu_{32.5}Si_{17.3}$, which follows the reported composition of the Laves phase in the Mn-Cu-Si system.[10] Two more alloys were prepared after the recognition of the true single phase region of the Laves phase from that alloy: one with a nominal composition $Mn_{33}Cu_{50}Si_{17}$ by assuming that an ordered crystal structure could be reached (Mn at the $4f$ site, Cu at the $6h$ site, and Si at the $2a$ site) and the other one with $Mn_{33}Cu_{55}Si_{12}$ based on the composition from the electron probe microanalysis (EPMA) measurements for the previous two samples. Only two alloys with compositions $Mn_{33.3}Ni_{41.7}Si_{25}$ and $Mn_{23}Ni_{51}Si_{26}$ in the Mn-Ni-Si system were prepared. The alloys with the nominal compositions $Mn_{33}Cu_{55}Si_{12}$ ($MnCu_{1.65}Si_{0.35}$) and

$Mn_{33.3}Ni_{41.7}Si_{25}$ ($MnNi_{1.25}Si_{0.75}$) were used for crystal structure, transport property and magnetic property investigations since the impurities are less than 1 vol.%.

All alloys (1 g each) were arc-melted on a water-cooled Cu hearth from high purity elements (more than 99.99 wt.%) in Ti-gettered argon. A slight excess of Mn was used to compensate its evaporation during melting. Each alloy was weighed after melting and Mn was added, if necessary, until the nominal composition was achieved. A part of each alloy was sealed in a vacuum quartz tube and annealed at 800 °C for 10 days prior to quenching into cold water. In addition, for the alloys $Mn_{50.2}Cu_{32.5}Si_{17.3}$ and $Mn_{33}Cu_{55}Si_{12}$, the same annealing conditions, as reported in the literature (700 °C, 10 days),[10] were used to check the phase constitutions. Details of the various techniques for characterization of composition and crystal chemistry including LOM, EPMA, XPD, and single crystal diffraction (XSCD, single crystals were mechanically isolated from crushed alloys) have been described in our previous papers.[20,21]

Neutron diffraction was performed at room temperature on the high-resolution diffractometer HRPT[22] at the SINQ spallation source of the Paul Scherrer Institut (Switzerland). The diffractometer was used in high-intensity mode ($\Delta d/d \leqslant 2 \times 10^{-3}$) with a neutron wavelength $\lambda_{\text{neutron}} = 0.14940$ nm and 2θ varying from 3.55° to 163.8°.

B. Physical properties

Electrical resistivity below room temperature was measured in a standard four-probe ac bridge technique in a home-made device. Seebeck coefficient measurements were carried out with a differential method. The absolute values $S_x(T)$ were calculated by the equation: $S_x(T) = S(T) - \frac{V_{\text{Pb}}/x}{\Delta T}$, where S is the absolute Seebeck coefficient of lead and V_{Pb}/x is the thermally induced voltage across the sample, depending on the temperature gradient ΔT. Above room temperature, electrical resistivity and Seebeck coefficient were measured with a ZEM-3 (ULVAC-Riko, Japan) equipment.

Temperature-dependent magnetization $M(T)$ and isothermal magnetization $M(H)$ measurements were performed in a 6-T CRYOGENIC SQUID magnetometer (3 K to room temperature) and on a QuantumDesign 9-T vibrating sample magnetometer (VSM) equipped with a VSM oven operating up to 900 K. Supplementary measurements of ac susceptibility were carried out with a commercial ac susceptometer (Lakeshore 7000) with an ac-field amplitude of 200 A/m and a frequency of 133 Hz (4.2 K to room temperature). Specific heat measurements were made in a home-made calorimeter in the temperature range 3–20 K on 0.5–0.6-g samples employing an adiabatic step heating technique.

Nuclear magnetic resonance (NMR) measurements were performed in a pulse spectrometer utilizing Fourier transforms of phase-cycle averaged Hahn spin echos from optimized pulse sequences with typical pulse durations of 3.0 μs at 30-μs intervals. We took spectra of Cu in $MnCu_{1.65}Si_{0.35}$ at fixed frequencies between 19.7 and 65.1 MHz and at temperatures between 1.8 and 300 K, and those of (defect site) Mn and Si in $MnNi_{1.25}Si_{0.75}$ at $T = 1.8$ K, all pointwise in variable applied field mode. A search for a zero-field Mn resonance at room temperature between 15 and 220 MHz was not successful.

For band-structure calculations, we used full potential density functional theory implemented in the WIEN2K program package with the generalized gradient approximation functional of Perdew *et al.* for the exchange potential.[23,24] The muffin-tin radii were set to touching spheres and stable values for the properties discussed below were found in calculations with $21 \times 21 \times 10$ k points or more in the irreducible wedge of the Brillouin zone. Where an on-site orbital potential U was introduced we used effective values $U_{\text{eff}} = U - J$ for the transition metal d electrons.[25,26] Convergence criteria for self-consistency were energy, charge, and the magnetic moments at Mn, which give rise to the nuclear Fermi-contact hyperfine fields calculated within the code[27] and which are compared to the experimental results.

III. RESULTS AND DISCUSSION

A. Chemical properties

1. *Phase relations*

Investigation of the alloy $Mn_{50.2}Cu_{32.5}Si_{17.3}$ reveals a discrepancy in phase constitution when compared to the literature data.[10] Figure 1 shows the XPD pattern and scanning electron microscope (SEM) image (inset) of this alloy after annealing (800 °C, 10 days). At first glance, the XPD pattern is compatible with the $MgZn_2$-type Laves phase, with only two very weak foreign peaks. However, the SEM image unambiguously shows that the volume percentage of the secondary (black) phase is more than 30%. Peak overlap is supposed to be the reason for the conclusion of an odd stoichiometry for the Laves phase in this system.[9,10] Model calculations of x-ray intensities are of little help, since the scattering length of Cu is similar to that of Mn.

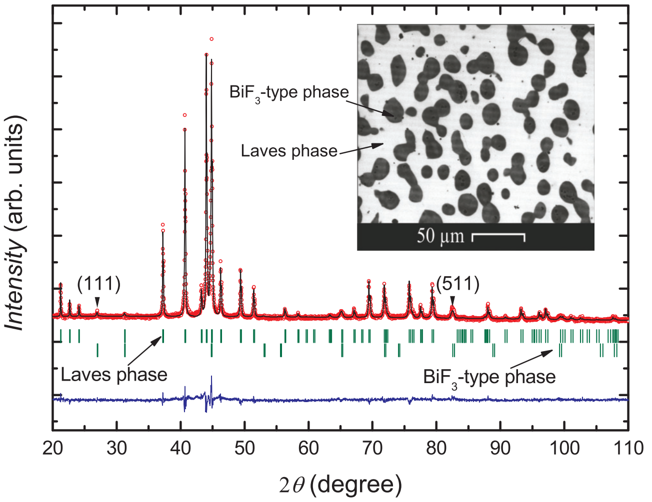

FIG. 1. (Color online) XPD pattern and SEM image (inset) for the annealed (800 °C, 10 days) sample $Mn_{50.2}Cu_{32.5}Si_{17.3}$. The red circles denote the experimental data points, the black line is the fit based on two phase contributions, the $MgZn_2$-type Laves phase and the BiF_3-type phase. The Bragg positions for each phase were indicated by vertical bars. In the SEM image, two phases can be recognized, with the white phase as the Laves phase and the black phase as the BiF_3-type phase.

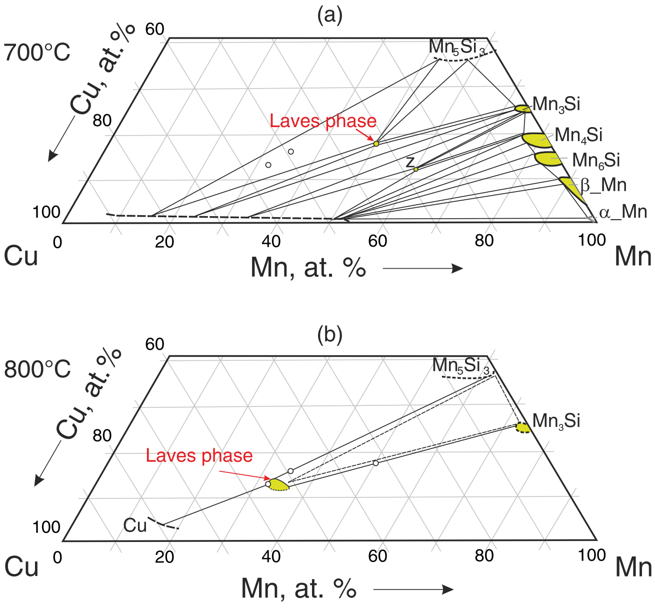

FIG. 2. (Color online) Isothermal section of the Mn-Cu-Si system (a) at 700 °C after Ref. 10 and (b) at 800 °C from this work. The location of the Laves phase region in (b) is quite different from that in (a).

EPMA measurements for this annealed sample yield that the composition of the main phase (white phase in Fig. 1) is $Mn_{36.6}Cu_{51.8}Si_{11.6}$, which has the stoichiometry of an AB_2 Laves phase, with the B element substituted by Si. The secondary phase has a composition $Mn_{74.0}Cu_{1.5}Si_{24.5}$, which can be considered as a limited solid solubility of Cu in the binary phase Mn_3Si (BiF_3-type).

Rietveld refinement for the XPD data of this sample with the structure model derived from the single crystal x-ray data (see Sec. III A2), i.e., Mn situated at the $4f$ site, Cu and Si sharing the $2a$ and $6h$ sites for the Laves phase, and the Mn_3Si as the secondary phase resulted in acceptable reliability factors, reasonable temperature factors at each site in the crystal structure and a composition comparable with that from the EPMA measurements for the Laves phase (see Fig. 1). The sample annealed at 700 °C for 10 days has the same phase constitution as the sample annealed at 800 °C, with a slight difference in the composition of the Laves phase (less than 1 at.% for the Mn atom).

Since the Laves phase in the Mn-Cu-Si system has a "normal" composition, a completely ordered structure might be expected in the sample of a nominal composition Mn_2Cu_3Si ($Mn_{33}Cu_{50}Si_{17}$). However, the XPD data and EMPA results of the annealed sample $Mn_{33}Cu_{50}Si_{17}$ (800 °C, 10 days) disclosed two phases: Laves phase [$Mn_{32.5}Cu_{54.0}Si_{13.5}$, $a = 0.48120(4)$ nm and $c = 0.78508(9)$ nm] in equilibrium with the Mn_5Si_3-type phase [$Mn_{62.8}Cu_{1.2}Si_{36}$, SP: $P6_3/mcm$, $a = 0.6911(3)$ nm and $c = 0.48179(6)$ nm].

Obviously, the results from the previous two alloys suggested that the Laves phase has a lower Si content. A new alloy with a nominal composition $Mn_{33}Cu_{55}Si_{12}$ was prepared. The investigation indicated that the annealed sample is an almost single phase alloy, with a secondary phase of $Cu_{1-x}Mn_x$ [measured composition: $Mn_{16.5}Cu_{79.3}Si_{4.2}$, see Fig. 3(b)]. The amount of the secondary phase derived from the Rietveld refinement of the XPD data is less than 1 Vol.%.

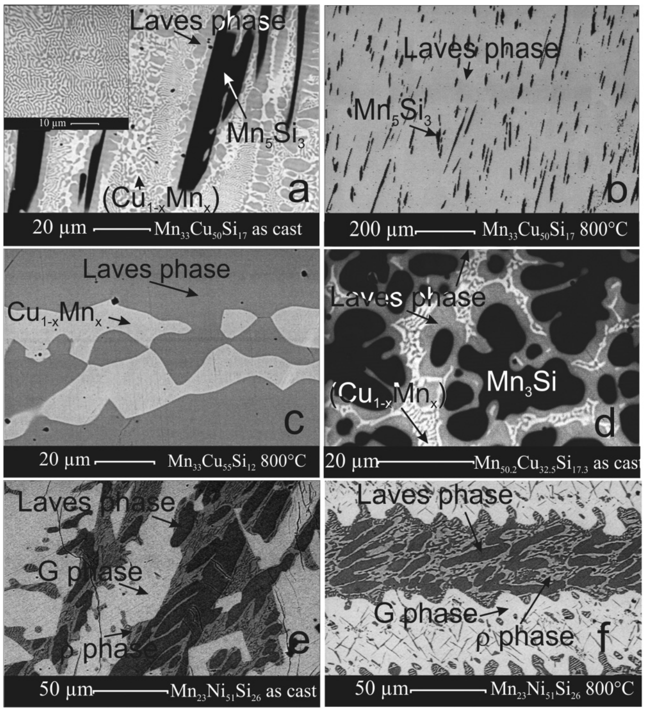

FIG. 3. SEM images for (a) $Mn_{33}Cu_{50}Si_{17}$, as cast state, (inset) eutectic area enlarged; (b) $Mn_{33}Cu_{50}Si_{17}$, annealed state (800 °C); (c) $Mn_{33}Cu_{55}Si_{12}$, annealed state (800 °C), extreme case (to measure the composition of the secondary phase); (d) $Mn_{50.2}Cu_{32.5}Si_{17.3}$, as cast state; (e) and (f) $Mn_{23}Ni_{51}Si_{26}$, as cast and annealed states, respectively.

Based on these results the phase relations at 800 °C associated with the Laves phase in the Mn-Cu-Si system were established as shown in Fig. 2(b). In contrast to literature data,[10] the Laves phase region extends from 32.5 to 36.7 at.% Mn and from 11.5 to 13.5 at.% Si, which is far from $Mn_{50.2}Cu_{32.5}Si_{17.3}$. The Laves phase forms tie lines to the phases Mn_3Si, Mn_5Si_3, and $Cu_{1-x}Mn_x$. More data are needed to confirm the equilibrium between the Laves phase, the Mn_3Si phase, and the Mn_5Si_3 phase and to complete the partial isothermal section.

The SEM images of these compounds in different states are shown in Figs. 3(a)–3(d). A completely different microstructure in the annealed sample compared with that in the as cast sample [for instance, see Figs. 3(a) and 3(b)] suggests that the Laves phase in the Mn-Cu-Si system forms incongruently.

In contrast to the Mn-Cu-Si system, the Laves phase in the Mn-Ni-Si system crystallizes congruently: the alloy $Mn_{33.3}Ni_{41.7}Si_{25}$ was practically single phase in the as cast and annealed state (800 °C), only a tiny amount of a secondary phase with a composition $Mn_{20.1}Ni_{54.6}Si_{24.4}$ was recognized as the G phase (Th_6Mn_{23}-type, SG: $Fm\bar{3}m$).[28] The SEM images of the as cast and annealed sample $Mn_{23}Ni_{51}Si_{26}$ show the G phase, Laves phase in equilibrium with the so-called ρ phase [$Mn_{15.0}Ni_{52.7}Si_{23.3}$, unknown structure type,[14] see Figs. 3(e) and 3(f)]. Analysis of these alloys thus confirmed the phase relations shown in Ref. 14.

2. *Crystal structure*

X-ray single-crystal structure determination via direct methods confirmed for both single crystals $Mn_{33}Cu_{55}Si_{12}$ and $Mn_{33.3}Ni_{41.7}Si_{25}$ isotypism with the $MgZn_2$-type Laves phase (C14) with space group $P6_3/mmc$. Direct methods delivered a structure solution suggesting Mn atoms at the $4f$ site and Cu/Si atoms covering two lower but different electron densities of the $6h$ and $2a$ sites. Since the Laves phases in both systems comply with the "ideal" formula AB_2, and in the $MgZn_2$-type Laves phase, the large electropositive element A typically occupies the $4f$ site and B atoms adopt the $2a$ and $6h$ sites (this is true even for a composition deviating strongly from the standard AB_2 stoichiometry[21]). Thus the larger electropositive Mn should occupy the $4f$ site and the Cu and Si atoms share the $2a$ and $6h$ sites (which was also suggested in Refs. 10 and 14 but in different ratio). Introducing anisotropic atom displacement parameters (ADPs) this model successfully refines to residual electron densities of $\pm 1.1\, e^-/10^{-3}$ nm^3 for $Mn_{33}Cu_{55}Si_{12}$ and $\pm 1.2\, e^-/10^{-3}$ nm^3 for $Mn_{33.3}Ni_{41.7}Si_{25}$, and residual values as low as $R_F = 0.014$ and $R_F = 0.019$ for $Mn_{33}Cu_{55}Si_{12}$ and $Mn_{33.3}Ni_{41.7}Si_{25}$, respectively (see Table I). As the transition metals involved exhibit similar x-ray scattering factors, a test was made to prove the atom site distribution by exchanging Mn and Cu atoms, i.e., placing Cu atoms at the $4f$ site and Mn sharing the $6h$ site with Si/Cu. The refinement of this model yielded an R value of 0.101 in combination with residual electron densities of $\pm 6\, e^-/10^{-3}$ nm^3 and therefore clearly documents that the most electropositive and the large Mn-atom occupies the $4f$ site.

A subsequent Rietveld refinement of the XPD data based on the results of the XSCD and with the corresponding secondary phases (Mn_3Si for $Mn_{33}Cu_{55}Si_{12}$ and the G phase for $Mn_{50.2}Ni_{32.5}Si_{17.3}$) confirmed this model, with reliability factors $R_F = 0.050$ and $R_I = 0.045$ for $Mn_{33}Cu_{55}Si_{12}$, as well as $R_F = 0.048$ and $R_I = 0.040$ for $Mn_{33.3}Ni_{41.7}Si_{25}$, respectively. The results show that the Si atoms in both Laves phases occupy preferably the $6h$ site, and the refined composition is very close to that measured by EPMA.

Neutron diffraction provides a perfect tool to determine the site preferences of Mn by making use of its negative neutron scattering length. However, as will be seen in Sec. III A3, both compounds are antiferromagnetic at room temperature. The intensity contribution from the magnetic phase in the ND pattern adds free variables to the structure determination, i.e., both magnetic structure and nuclear structure need to be refined simultaneously.

3. *Magnetic structure*

Rietveld refinement of the ND data for both compounds based on the initial structure model derived from XSCD data were not immediately successful and it was concluded that magnetic ordering might contribute to the Bragg peaks being responsible for the discrepancies between the structure calculations and the observations. Magnetic susceptibility and nuclear magnetic resonance (NMR) measurements (see Secs. III B3 and III B4) confirmed the magnetic ordering in both samples at room temperature. An inspection of the ND pattern and the calculated pattern based on the structure model from XSCD data discloses that only the intensity of (10l) reflections was enhanced. No additional peak from the magnetic phase appears in the ND pattern, indicating that the magnetic cell has the same size as the nuclear one and thus the propagation k = [000]. With this propagation vector by using the program SARAH,[30] we were able to obtain possible irreducible representations. The final magnetic structure was solved by "trial and error" from Rietveld refinement in FULLPROF[31] with the irreducible representations and the nuclear structure taken from the XSCD data. Our results show that in both Laves phases only the Mn atoms at the $4f$ site carry magnetic moments, which are aligned antiferromagnetically along the c axis (see Fig. 4, inset). The resultant magnetic moment of Mn in $Mn_{33}Cu_{55}Si_{12}$ is $2.7\mu_B$, slightly smaller than that of $2.9\mu_B$ in $Mn_{33.3}Ni_{41.7}Si_{25}$. Both values are comparable to the magnetic moment of Mn in the cubic G phase $Mn_6Ni_{16}Si_7$ ($2.7\mu_B$/Mn).[19] Final refinements for both nuclear and magnetic structures reveal no significant change in the nuclear structure, confirming the site preferences for Mn, Ni, Cu, and Si in the Laves phases. The refinements yield the reliability factors $R_B = 0.060$, $R_F = 0.050$, and $R_M = 0.080$ for $Mn_{33}Cu_{55}Si_{12}$ as well as $R_B = 0.045$, $R_F = 0.070$, and $R_M = 0.076$ for $Mn_{33.3}Ni_{41.7}Si_{25}$, respectively.

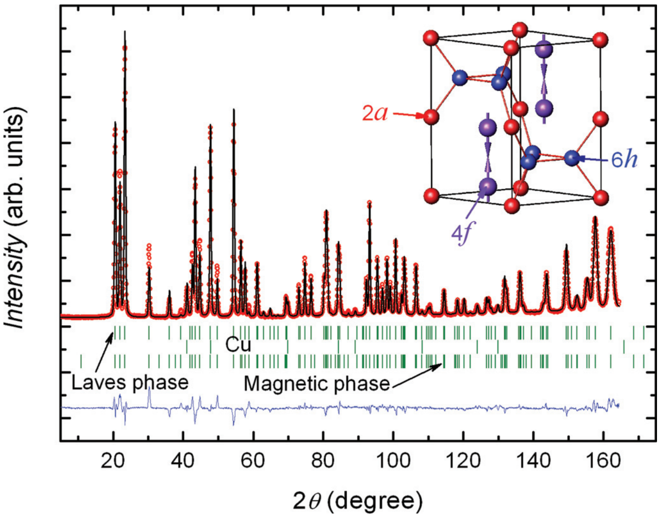

FIG. 4. (Color online) Rietveld refinement of the ND data for annealed (800 °C, 10 days) $Mn_{33}Cu_{55}Si_{12}$, (inset) magnetic structure derived from this refinement. The red circles are observations. The black line is the model calculation fit. The magnetic phase is considered as a separate phase with space group $P\bar{1}$. The reliability factors of the refinement are $R_B = 0.060$, $R_F = 0.050$, and magnetic $R_M = 0.080$. In the magnetic structure, only the Mn atoms (in violet color, at the $4f$ sites) are identified to carry magnetic moments orientated antiferromagnetically along the c axis.

B. Physical properties

1. *Low temperature specific heat*

The temperature-dependent specific heat, C_p, of $MnCu_{1.65}Si_{0.35}$ ($Mn_{33}Cu_{55}Si_{12}$) and $MnNi_{1.25}Si_{0.75}$ ($Mn_{33.3}Ni_{41.7}Si_{25}$) is displayed in Fig. 5 as C_p/T vs T^2 with linear regressions (black lines), revealing a simple $C_p(T) = \gamma T + \beta T^3$ behavior at lowest temperatures. In the

TABLE I. Structure data derived from the XSCD (radiation: Mo, K_α,$\lambda = 0.071069$ nm, $2^\circ < 2\theta < 72.45^\circ$) data for $Mn_{33}Cu_{55}Si_{12}$ and $Mn_{33.3}Ni_{41.7}Si_{25}$ ($MgZn_2$-type, space group: $P6_3/mmc$). The data were standardized by the program STRUCTURE TIDY.[29]

Compound	$Mn_{33}Cu_{55}Si_{12}$	$Mn_{33.3}Ni_{41.7}Si_{25}$
refined composition	$Mn_{33.3}Cu_{51.7}Si_{15}$	$Mn_{33.3}Ni_{42.3}Si_{24.4}$
composition from EPMA	$Mn_{33.3}Cu_{53.8}Si_{12.9}$	$Mn_{33.5}Ni_{42.3}Si_{24.2}$
a, c (nm)	0.48208(2), 0.78605(3)	0.47564(2), 0.75131(3)
Reflections	$160 \geqslant 4\sigma\ (F_o)$ of 172	$150 \geqslant 4\sigma\ (F_o)$ of 162
Number of variables	15	15
$R_F = \sum \lvert F_o - F_c \rvert / \sum F_o$	0.014	0.019
ωR^2	0.035	0.080
R_{int}	0.066	0.066
GOF	1.130	0.718
Atomic parameters		
Mn in $4f(1/3,2/3,z),z$	0.56332(5)	0.56435(9)
U_{ij} $10^2(\text{nm}^2)$	$U_{11} = U_{22} = 0.0089(1)$, $U_{33} = 0.0088(2), U_{12} = 0.0044(1)$	$U_{11} = U_{22} = 0.0087(3)$, $U_{33} = 0.0063(4), U_{12} = 0.0043(2)$
M1 at $6h(x,2x,1/4),x$	0.17061(3)	0.17100(5)
Occ.	4.35(2)Cu + 1.65Si	4.09(2)Ni + 1.91Si
U_{ij} $10^2(\text{nm}^2)$	$U_{11} = 0.0096(1), U_{22} = 0.0055(2)$, $U_{33} = 0.0085(2), U_{12} = 0.0027(1)$	$U_{11} = 0.0099(3), U_{22} = 0.0059(3)$, $U_{33} = 0.0062(4), U_{12} = 0.0030(2)$
M2 at $2a(0,0,0)$, Occ.	1.85(1)Cu + 0.15Si	0.99(1)Ni + 1.01Si
U_{ij} $10^2(\text{nm}^2)$	$U_{11} = U_{22} = 0.0115(2)$, $U_{33} = 0.0058(2), U_{12} = 0.0057(1)$	$U_{11} = U_{22} = 0.0181(4)$, $U_{33} = 0.0048(5), U_{12} = 0.0091(2)$
Interatomic distances (nm); standard deviation is less than 0.0005 nm		
Mn-3M1	0.2183	0.2714
Mn-6M1	0.2822	0.2757
Mn-3M2	0.2827	0.2788
Mn-1Mn	0.2935	0.2790
Mn-3Mn	0.2956	0.2911
M1-2M1	0.2353	0.2316
M1-2M2	0.2427	0.2348
M1-2M1	0.2467	0.2440
M1-2Mn	0.2813	0.2714
M1-4Mn	0.2822	0.2757
M2-6M1	0.2427	0.2348
M2-6Mn	0.2827	0.2788

case of simple metals, γT represents the T-linear electronic contribution and βT^3 the lattice contribution with β being related to the low-temperature value of the Debye temperature $\Theta_D^{LT} = (1944 \times N/\beta)^{1/3}$, where $N = 3$ is the number of atoms per formula unit of these Laves phases. The linear regressions in Fig. 5 yield the experimental values of the Sommerfeld coefficients $\gamma = 3.24$ and 12.73 mJ/(mol K^2) for $MnNi_{1.25}Si_{0.75}$ and $MnCu_{1.65}Si_{0.35}$, respectively. The γ value of $MnNi_{1.25}Si_{0.75}$ is reasonably comparable with that from band-structure calculations (see Sec. III B5). However, the calculated γ value of $MnCu_{1.65}Si_{0.35}$ is much smaller even than that of $MnNi_{1.25}Si_{0.75}$, indicating a significant magnetic contribution to the specific heat of $MnCu_{1.65}Si_{0.35}$.

The corresponding T^3 coefficients $\beta = 48.88$ μJ/(mol K^4) for $MnNi_{1.25}Si_{0.75}$ and $\beta = 111.3$ μJ/(mol K^4) for $MnCu_{1.65}Si_{0.35}$ yield $\Theta_D = 492.3$ and 374.2 K, respectively. These Debye temperatures, however, possibly underestimate the intrinsic values because the βT^3 specific heat component may include contributions from antiferromagnetic spin wave excitations.

2. *Electrical resistivity and Seebeck coefficient*

The temperature-dependent electrical resistivity $\rho(T)$ and Seebeck coefficient $S(T)$ for the polycrystalline samples $MnCu_{1.65}Si_{0.35}$ and $MnNi_{1.25}Si_{0.75}$ are shown in Figs. 6(a) and 6(b), respectively. As it is obvious from these figures, $\rho(T)$ of both samples exhibit a quite uncommon temperature dependence, with broad ranges of negative values of $d\rho/dT$. A pronounced change of the slopes of $\rho(T)$ (see the insets in both panels) marks the magnetic phase transition temperature. These temperatures coincide with the anomalies seen in the $S(T)$ data, too. The most prominent feature in the temperature-dependent electrical resistivity, however, is the extended range, where the resistivity decreases with increasing temperature. Such a behavior, in principle, is reminiscent of an insulating

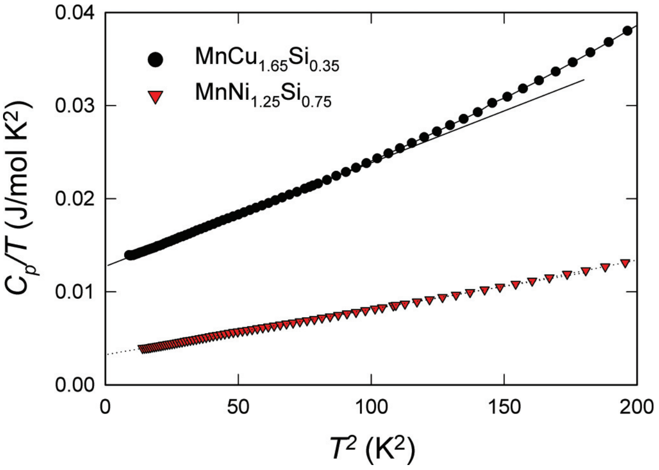

FIG. 5. (Color online) Temperature-dependent specific heat as C/T vs T^2 for MnNi$_{1.25}$Si$_{0.75}$ and MnCu$_{1.65}$Si$_{0.35}$. The black solid and dotted lines indicate linear regressions of the low-temperature data as discussed in the text.

state with the Fermi energy being in or close to a gap in the electronic density of states. DFT calculations (see below) in the context of the finite Sommerfeld values observed from the heat capacity data, however, strongly indicate a metallic state. Weak localization effects of conduction electrons in intermetallic compounds are one of the rare mechanisms, able to explain a negative slope of $d\rho/dT$ in this range. Localization is expected to be triggered by disorder owing to the site interchanges of Cu(Ni) and Si. In order to model $\rho(T)$ of both compounds in terms of weak localization, a set of dimensional dependent equations, worked out by Lee and Ramakrishnan,[32] are considered. For the three-dimensional case, this equation reads

$$\sigma^{3D}(T) = \sigma_0 + \frac{e^2}{\hbar\pi^3}\frac{1}{a}T^{p/2}. \tag{1}$$

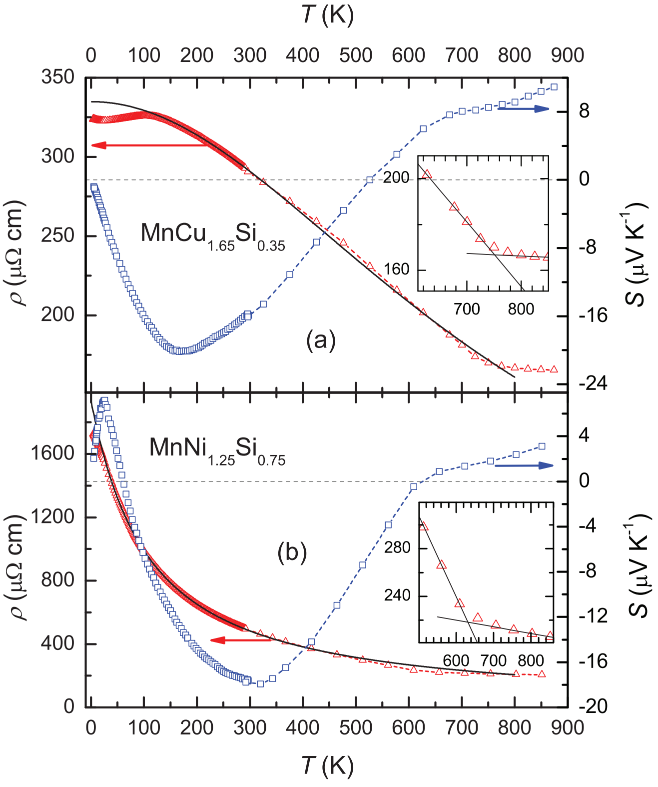

FIG. 6. (Color online) Temperature-dependent electrical resistivity and Seebeck coefficient for (a) MnCu$_{1.65}$Si$_{0.35}$ and (b) MnNi$_{1.25}$Si$_{0.75}$. Insets zoom in $\rho(T)$ in the temperature range with a pronounced change of slope. The solid lines are fits for the electrical resistivity (see text).

Fitting the data of Figs. 6(a) and 6(b) in terms of Eq. (1) for those temperatures where $d\rho/dT < 0$, reveals $p \approx 4$ and 2, respectively. Here, p is an exponent used to parametrize the temperature dependence of the inelastic scattering length L_i through $L_i \propto T^{-p/2}$. a is some microscopic length scale of the problem, such as the inverse Fermi wave number. $p = 2$ typically refers to predominant electron-phonon interactions in the system. The substantial difference of this exponent in the Cu- and the Ni-based compounds therefore indicates that the scattering of the charge carrying electrons is quite different in both materials, hence also referring to differences in the interaction of electrons with magnetic moments of both systems. It should be noted that changes of the magnetic structure in the ordered phase or the crossover to the paramagnetic phase influence the electron-magnetic moment interaction and thus the temperature-dependent electrical resistivity as well.

The onset of long-range antiferromagnetic order can be accompanied by so-called superzone boundary effects, where due to the opening of a gap in the electronic density of states, a reduction of the charge carrier density occurs; consequently, the conductivity decreases. Superzone boundaries operate equally on impurity, phonon as well as magnetic moment scattering. In general, however, these effects occur if magnetic ordering exhibits a periodicity different from that of the lattice.[33] Since the magnetic propagation vector is zero for both MnCu$_{1.65}$Si$_{0.35}$ and MnNi$_{1.25}$Si$_{0.75}$, superzone boundary effects are rather unlikely to explain the negative $d\rho/dT$ observed right below magnetic ordering.

The temperature-dependent Seebeck coefficient $S(T)$ [see Figs. 6(a) and 6(b)] exhibits a quite complicated overall behavior, where changes from positive to negative values of the thermopower are present. In the case of simple materials, positive and negative $S(T)$ values would refer to a dominance of holes or electrons, respectively, as the principal charge carriers. Simple metals, however, would be accompanied by an almost linear temperature dependence of $S(T)$ and their absolute values would be inversely proportional to the charge carrier density. In terms of Mott's formula of thermopower, $S(T) = 1/N(E) \cdot \partial N(E)/\partial E|_{E=E_F}$, small changes of the energy derivative of $N(E)$ can distinctly influence the overall behavior of $S(T)$. Nevertheless, the clear changes of slopes of $S(T)$ at the magnetic phase transition temperatures for both MnCu$_{1.65}$Si$_{0.35}$ and MnNi$_{1.25}$Si$_{0.75}$ apparently evidence magnetic contributions; modifications of these contributions, in fact, will have a distinct impact on the temperature-dependent thermopower.

3. *Magnetic properties*

The results of field and temperature-dependent dc magnetic susceptibility measurements, M/H, on MnNi$_{1.25}$Si$_{0.75}$ and

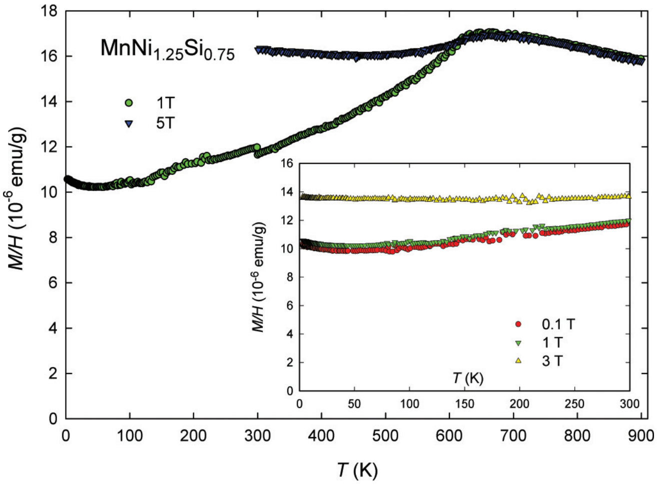

FIG. 7. (Color online) Temperature-dependent dc magnetic susceptibility $M/H(T)$ for $MnNi_{1.25}Si_{0.75}$ measured at various fields as labeled. Data below and above room temperature were obtained by SQUID and VSM techniques, respectively. The inset zooms in on the low-temperature susceptibility data.

$MnCu_{1.65}Si_{0.35}$ are shown in Figs. 7 and 8, respectively. The susceptibility maximum of $MnNi_{1.25}Si_{0.75}$ at 630 K corresponds to an antiferromagnetic instability of the Néel temperature T_N of the antiferromagnetic ordering. The 1-T susceptibility data reach a value near about 2/3 of $M/H(T_N)$ at lowest temperatures as expected for a simple antiferromagnetic state. While the 0.1- and 1-T susceptibility of $MnNi_{1.25}Si_{0.75}$ scale reasonably well, 3- and 5-T susceptibility data—up to T_N—clearly exceed the susceptibility measured at lower fields. This observation is related to a metamagnetic spin flop transition of the anitferromagnetic spin structure which is seen in the isothermal magnetization data $M(H)$ at 12 K shown in Fig. 9(a). The onset of the metamagnetic transition of $MnNi_{1.25}Si_{0.75}$ is revealed by a kink of the $M(H)$ curve at about 2.2 T.

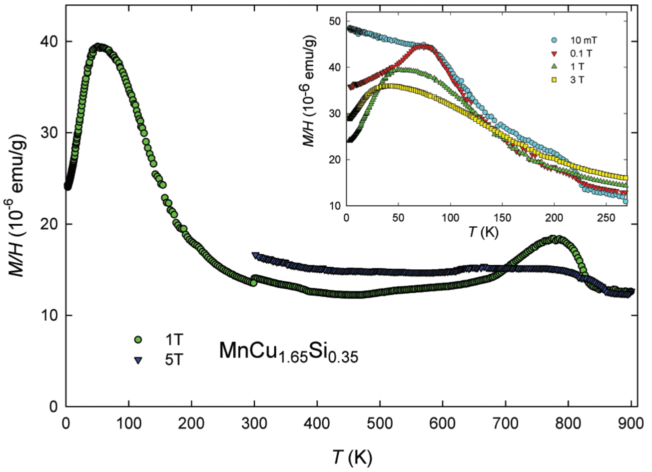

FIG. 8. (Color online) Temperature-dependent dc magnetic susceptibility M/H for $MnCu_{1.65}Si_{0.35}$ measured at various fields as labeled. Data below and above room temperature were obtained by SQUID and VSM techniques, respectively. The inset zooms in on the low-temperature susceptibility data.

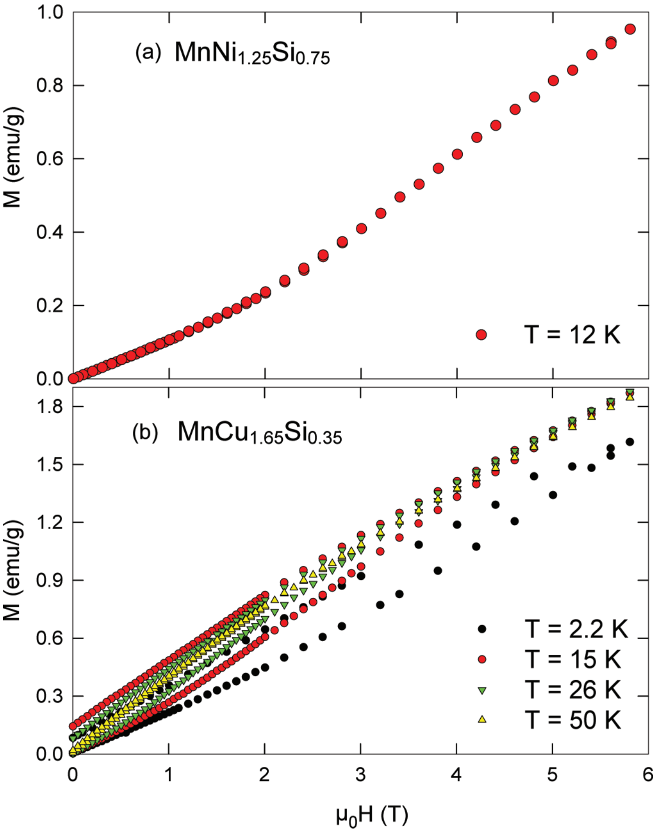

FIG. 9. (Color online) Isothermal magnetization measurements $M(H)$ for (a) $MnNi_{1.25}Si_{0.75}$ and (b) $MnCu_{1.65}Si_{0.35}$ measured at various temperatures. Each $M(H)$ cycles on $MnCu_{1.65}Si_{0.35}$ was measured after zero-field cooling from above 120 K.

The temperature-dependent susceptibility of $MnCu_{1.65}Si_{0.35}$ in Fig. 8 displays a distinct anomaly at around 800 K, which indicates the onset of long range magnetic order. According to room temperature ND (see Sec. III A3) and NMR studies (see Sec. III B4), an antiferromagnetic state is established thereby. The less trivial temperature dependencies with crossing points of the 1- and 5-T susceptibilities and further, field-dependent susceptibility anomalies below room temperature are indicative of a more complex nature of the antiferromagnetic state in $MnCu_{1.65}Si_{0.35}$ than in $MnNi_{1.25}Si_{0.75}$. The low-temperature anomalies highlighted in the inset of Fig. 8 at about 80 K at lowest fields (0.01 and 0.1-T susceptibilities and also in the ac susceptibility which is not shown) indicate a spin re-orientation transition of the antiferromagnetic state, which is also observed by NMR studies, suggesting a gradual transition between two different AF structures (see Sec. III B4). Another anomaly occurring at about 230 K, which is clearly seen for the 10-mT data of $MnCu_{1.65}Si_{0.35}$ and is smeared out in higher fields, may originate from traces of a ferromagnetic impurity. Isothermal magnetization $M(H)$ measurements of $MnCu_{1.65}Si_{0.35}$ displayed in Fig. 9(b) reveal a hysteresis behavior of the magnetization at lowest temperatures, which disappears at elevated temperatures where a distinct metamagnetic anomaly appears to be absent [see the isothermal magnetization $M(H)$ at 50 K and the

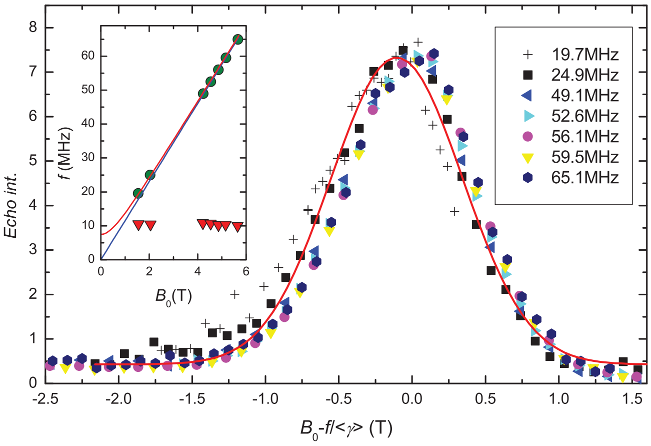

FIG. 10. (Color online) Cu NMR spin-echo field sweep spectra in $\mathrm{MnCu_{1.65}Si_{0.35}}$ at $T = 4.2$ K and at spectrometer frequencies indicated in the figure, scaled to equal maximum intensity and shifted by the mean gyromagnetic ratio of Cu (see text). The inset shows the unshifted positions (green dots) and linewidth (red triangles) together with the γ line corresponding to the shift $\gamma_{\mathrm{Cu}} = 11.522$ MHz/T (blue line). The red line represents expected line positions in presence of a local field $B_\perp = 0.65$ T perpendicular to the applied field.

approximate scaling of the 1- and 5 -T susceptibility data up to about 700 K].

4. Nuclear magnetic resonance (NMR)

Figure 10 shows the Cu field sweep spin echo spectra of $\mathrm{MnCu_{1.65}Si_{0.35}}$ at 4.2 K at various frequencies. The spectra are normalized to equal intensity and field shifted by the resonance field $B_{\mathrm{shift}} = f/\gamma_{\mathrm{Cu}}$ of Cu for frequency f in a diamagnetic material (an abundance weighted mean for the two Cu isotopes: $\gamma_{\mathrm{Cu}} = 0.69 \times {}^{63}\gamma + 0.31 \times {}^{65}\gamma$ with ${}^{63}\gamma = 11.285$ MHz/T and ${}^{65}\gamma = 12.089$ MHz/T). The lines can be shifted to zero by this mean γ_{Cu}, indicating that this is a Cu resonance, neither originated by ^{55}Mn (${}^{55}\gamma = 10.5$ MHz/T) nor by ^{29}Si (${}^{29}\gamma = 8.458$ MHz/T).

There is a broad local field distribution (FWHM ≈ 1.0 T) at the Cu sites: the resonances of the Cu wire of the coil are delta peaks on this scale. The linewidth does not depend on the applied field (see inset), indicating that the local field distribution is not due to field induced moments from an inhomogeneous susceptibility, but due to static magnetic moments.

The magnetic structure is antiferromagnetic (AF) since at high frequency (applied field) there is no discernible shift from any net internal field. In addition, the static moments are not localized at the Cu-sites since this would lead to a large on-site hyperfine field. The fields are, therefore, transferred from an antiferromagnetic order at the Mn ($4f$) sublattice.

In a perfect lattice without Si, the Cu-sites are apparently located in positions where the transferred fields from the AF-structure cancel. The random distribution of the field strength leading to the Gaussian line shape is attributed to the distribution of Si at the $2a$ and $6h$ sublattices, which modifies the local moment of neighboring Mn ions as well as the hyperfine coupling of neighboring Cu to the Mn moments.

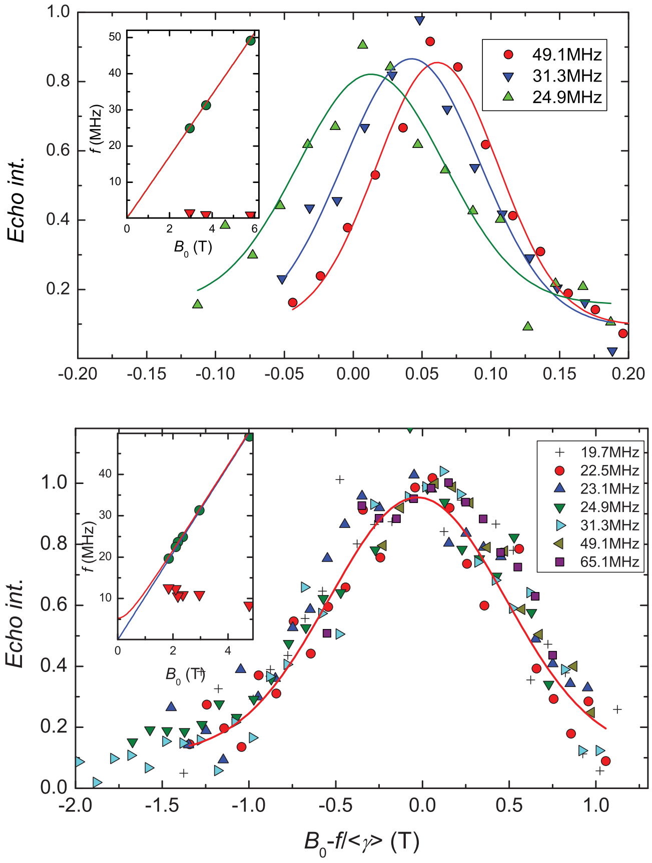

FIG. 11. (Color online) Si (top) and Mn (bottom) NMR spin-echo field sweep spectra in $\mathrm{MnNi_{1.25}Si_{0.75}}$ at $T = 1.8$ K and at spectrometer frequencies indicated in the figure, scaled to equal maximum intensity and shifted by the isotopic gyromagnetic ratio. The insets show the unshifted positions (green dots) and linewidth (red triangles) together with the γ line corresponding to the shift (blue lines). The red lines represent expected line positions in presence of a local field $B_\perp = 0.50$ T perpendicular to the applied field for Mn, and for a reduced effective $\gamma = 8.45$ MHz/T for Si (see text).

At low frequencies, the resonance is shifted slightly to frequencies larger than the ones corresponding to γ_{Cu} (see inset). The line positions can be well described by assuming that the mean local transferred field $B_\perp = 0.65$ T from the static moments is oriented perpendicular to the applied field. This is the most likely orientation in a powder pattern, and in the case when the lowest applied field is already above the spin-flop field at 4.2 K, this is also the thermodynamically stable orientation. We note that in our NMR measurements, we did not find evidence of the magnetic hysteresis which is, however, obviously observed in the low-temperature magnetization measurements. This indicates that the coupling constant to the moments responsible for the hysteresis is small enough to hide the corresponding line shift in the line width.

There is a small zero-field signal at all frequencies, indicated by the plateau of positive echo intensities on the low field side in the figure. This can be attributed either to Cu with transferred hyperfine fields of up to 6 T, or to Mn carrying rather small moments.

Figure 11 shows the corresponding spectra for Si and Mn in $\mathrm{MnNi_{1.25}Si_{0.75}}$ at 1.8 K. Both signals are small, more than two orders of magnitude smaller than the Cu signal in MnCu$_{1.65}$Si$_{0.35}$. With Si this is due to the small nuclear spin ($I = 1/2$) and, mostly, to the low natural abundance of ^{29}Si (4.7%). In addition, measurements are difficult due to a short spin-spin relaxation time t_2 ($\approx$50 μs) and a long spin-lattice relaxation time t_1 (above 10 s). For Mn, the small signal is surprising since the nuclear moment is larger ($I = 5/2$) than that of Cu and natural abundance is 100%.

The properties of both resonances in MnNi$_{1.25}$Si$_{0.75}$ are very similar to the ones of Cu in MnCu$_{1.65}$Si$_{0.35}$: A broad, field independent local field distribution without net component along the applied field allows to identify the contributing isotope by its gyromagnetic ratio γ. The linewidth of the Mn resonance is the same as that observed for Cu in MnCu$_{1.65}$Si$_{0.35}$. In addition, the perpendicular local field $B_\perp = 0.5$ T estimated from the measurements at low frequencies is the same within the error as that for the Cu resonance discussed above. We conclude, therefore, that MnNi$_{1.25}$Si$_{0.75}$ also is antiferromagnetic at low temperatures. The small Mn signal is ascribed to the substitution of Cu by less than 1% Mn at the 6h or 2a sites. The resonance from Mn at regular sites is shifted to completely different conditions by the large hyperfine field from local magnetic moments (see below).

The linewidth for the Si resonance is much smaller (FWHM $\approx$ 0.12 T). This is due to the missing 4s-band electron contribution to the transferred hyperfine fields from the magnetic sublattice and is confirmed by our DFT calculations (see Sec. III B5). The Si lines are narrow enough to detect a small field dependent line shift with respect to the Si resonance in a diamagnetic material. In the figure, the resonances are not shifted on top of each other by a shift with the diamagnetic $^{29}\gamma = 8.458$ MHz/T. An effective gyromagnetic ratio which is smaller by 1.1% improves the scaling but the significant non linear dependence on the applied field remains. This is expected since the modification of the internal field is due to demagnetization of the moment induced by the perpendicular antiferromagnetic susceptibility $\chi_\perp$ which is, in fact, nonlinear due to the spin-flop transition at 2.2 T [see Fig. 11(a)].

Figure 12 shows the linewidth Δ (FWHM) of the Cu field sweep spectra in MnCu$_{1.65}$Si$_{0.35}$ at 19.7 MHz at various temperatures between l-He and 300 K. It should be noted that the small signal intensities and the reduced spin-spin relaxation time t_2 in MnNi$_{1.25}$Si$_{0.75}$ make it difficult to do the same measurements at elevated temperatures. In the figure, Δ slightly increases with temperature and reaches a maximum at 20 K, which is possibly associated with the magnetic transition (more clear in the signal intensity (inset) and in the magnetic susceptibility data discussed above), then is almost independent and decreases with further increasing temperature. The decrease at $T > 150$ K is attributed to the decrease of Mn sublattice magnetization since the transferred hyperfine fields at the Cu nuclei are proportional to these magnetic moments. The red line is a fit of the temperature dependence of the Mn sublattice magnetization by using $M_{(T)} = M_{(T=0)}[1 - (T/T_x)^2]$ with a saturation transferred field linewidth $\Delta_{(T=0)} = 1.0$ T, and a characteristic energy $T_x = 550$ K associated with the antiferromagnetic spin wave spectrum. Comparison with the coefficient of the T^2 dependence of the sublattice magnetization for a bipartite AF with $S = 3/2$ calculated by Oguchi[34] or by Burr and Callen in a more general approach[35] yields an estimate of $J = 70$ K for the exchange integral, in reasonable agreement with $J = 85$ K estimated from $T_N = 850$ K and $z = 4$ antiferromagnetic couplings in simple mean field theory.[36]

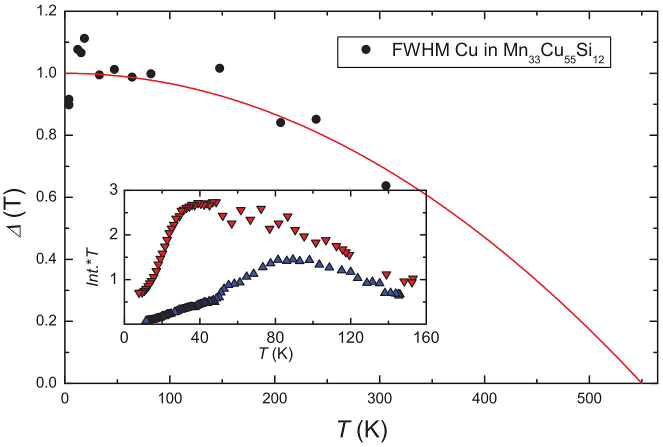

FIG. 12. (Color online) Temperature dependence of the linewidth (FWHM) of the Cu resonance in MnCu$_{1.65}$Si$_{0.35}$ compared to the temperature-dependent sublattice magnetization calculated within spin wave theory (line). The inset shows the spin echo intensity times temperature at 19.7 MHz and $B_0 = 1.68$ T with fixed excitation conditions optimized at 30 K (red down triangles, pulse distance 28 μs) and 80 K (blue up triangles, pulse distance 55 μs).

The unexpected temperature dependence of the signal intensity shown in the inset of Fig. 12 may indicate the nature of the transition below room temperature in MnCu$_{1.65}$Si$_{0.35}$ discussed above. Figure 13 shows the content of a primitive unit cell. Any doubling (or multiplying) of the unit cell by magnetic order would lead to nonvanishing transfered fields at the 2a or 6h positions, in contrast to what is observed in the Cu-NMR spectra. The magnetic unit cell is, therefore, identical to the crystallographic one, confirming the result from our neutron diffraction data above.

Within the unit cell there are three distinguishable compensated AF arrangements for the four Mn moments (besides orientations with respect to the lattice), denoted by AF-I and AF-IIa, AF-IIb in the figure. Each Mn has one Mn nearest neighbor at 0.2935 nm distance and three next nearest neighbors at slightly larger distance (0.2956 nm, see Table I). For AF-I both couplings to these neighbors are antiferromagnetic. For AF-IIa J_1 across the sheet of 6h-sites is antiferromagnetic

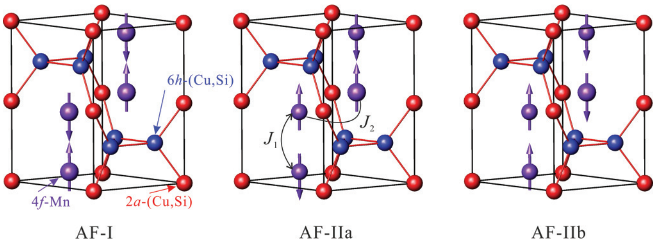

AF-I AF-IIa AF-IIb

FIG. 13. (Color online) Magnetic structures of MnCu$_{1.65}$Si$_{0.35}$ proposed from NMR for room temperature (AF-I, left) with a gradual transistion below ~80 K to AF-IIa (center) or AF-IIb (right), where AF-IIb appears to be favored by the temperature dependence of the Cu NMR signal intensity.

while J_2 across the sheet of $2a$ sites is ferromagnetic, and for AF-IIb the reverse is the case, namely, J_1 is ferro- and J_2 antiferromagnetic.

In the structure AF-I the transfered hyperfine fields at all $2a$ and $6h$ sites cancel if there is no Cu-, Si-site disorder. At the $6h$ sites, the compensation occurs between Mn nearest neighbors with spins coupled via J_1. At the $2a$ sites, the compensation occurs between Mn next nearest neighbors with exchange coupling J_2. There are three such pairs in the nearest neighbor shell of $2a$ sites. In the structure AF-IIa, the compensation at the $2a$ sites is expected to break down, while for AF-IIb the compensation at the $6h$ sites should fail.

The inset to Fig. 12 shows that with temperature decreasing from 160 K the signal first increases faster than $\text{Int} \times T =$ const predicted by the Curie law of nuclear magnetization. Comparison of the measurement with longer pulses and larger pulse distance (blue up triangles) and the one with shorter pulses and distances (red down triangles) indicates that the increase is not due to the increased spin-spin relaxation time but to the increase of the rf enhancement factor in the antiferromagnetic structure[37] with decreasing temperature. At 160 K, the pulse power is smaller than optimum in both settings. With lowering temperatures the enhancement factor increases, leading to better excitation conditions and larger signal intensities. The decrease in signal intensity at low temperature is, however, not related to this enhancement, since the echo shape stays constant. We interpret this as that a significant part of the Cu nuclei is shifted out of resonance by internal fields which develop in a gradual magnetic transition from AF-I at room temperature to AF-II below 20 K. This might also explain why the hysteresis behavior observed in the magnetization experiments is absent in NMR: if the moments responsible for the hysteresis are located in the AF-II phase their coupling to Cu nuclei in the AF-I phase detected in NMR would be expected to be small. While the low-temperature magnetism clearly requires further study one can conclude that above ≈80 K the local field distribution at the Cu nuclei corresponds to a magnetic structure where on average the transferred fields cancel. The magnetic structure at room temperature is, therefore, in accord with our neutron diffraction data for AF-I.

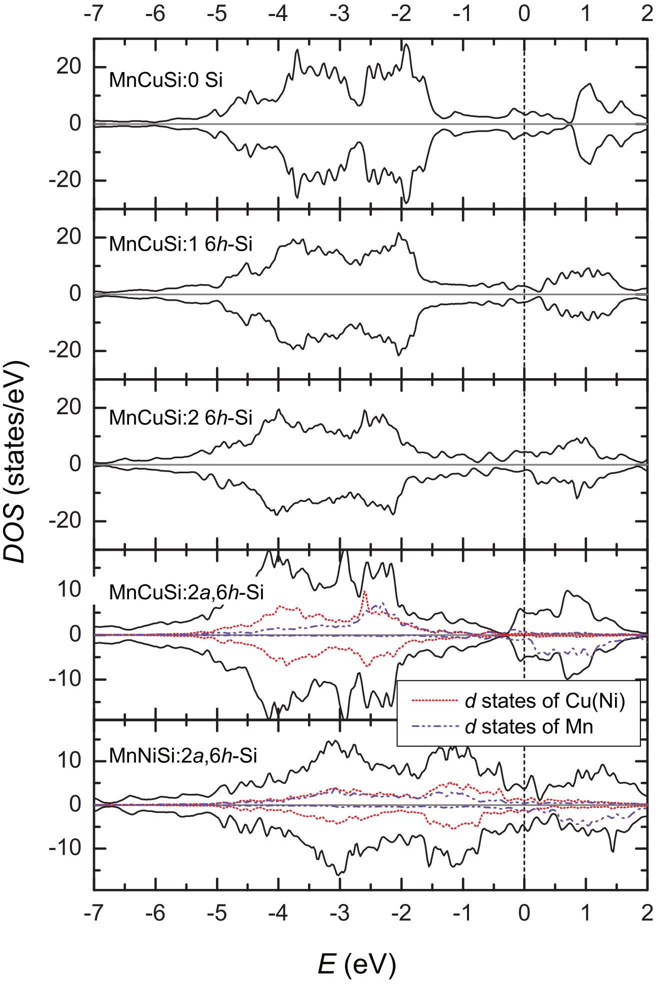

FIG. 14. (Color online) Total density of states of $\text{MnCu}_{1.65}\text{Si}_{0.35}$ in the magnetic AF-I phase for Si configurations as indicated in the panels, and for AF-I phase $\text{MnNi}_{1.25}\text{Si}_{0.75}$ with two Si in the unit cell (one at $2a$, the other at $6h$) in the bottom panel. The vertical dashed line marks the Fermi energy E_F. The two panels at the bottom show in addition the partial DOS projected on the d states of one of the Mn (blue, dashed), and Cu or Ni d states (red,dotted).

5. *Band-structure calculations*

Density functional theory calculations utilizing the WIEN2K code allow further insight into the origin of the physical properties of these materials. For the calculations, we approximate the random distribution of Cu (or Ni) and Si on the $6h$ and $2a$ sites in $\text{MnCu}_{2-x}\text{Si}_x$ by periodic structures. We restricted calculations to a unit cell of the same size as the one for the undistorted Laves phase, namely, four formula units of Mn(Cu,Si)_2. For $\text{MnCu}_{1.65}\text{Si}_{0.35}$, there are on average 1.43 Si in one unit cell, so we restricted our calculations to periodic structures with zero, one or two Si in the unit cell. The unit cell with the full space group $P6_3/mmc$ symmetry is obtained by placing two Si at the $2a$ sites and six Cu at the $6h$ sites (see Fig. 13). Placing only one Si at a $2a$ site reduces symmetry to space group $P3m1$, a single Si per unit cell at one $6h$ site reduces symmetry to the monoclinic space group Cm. All calculations discussed here were performed with the monoclinic space group.

Electronic densities of states (DOS) were calculated for a series of Si configurations, all with the AF-I magnetism (see Fig. 14). The total DOS shows that the Fermi energy is located at the upper end of a broad minimum between maxima from occupied and empty d bands in both spin channels (plotted as positive and negative DOS for the spin-up and spin-down channels, respectively). From the DOS projected on Mn and Ni or Cu sites in the two bottom panels it is seen that the Cu and Ni d states contribute only to the valence band maxima and to the small density at the Fermi energy, while the maxima in the DOS above E_F are related to Mn.

The influence of the Si substitutions on the DOS of $\text{MnCu}_{2-x}\text{Si}_x$ is relatively small, the situation in $\text{MnNi}_{2-x}\text{Si}_x$ is similar and therefore not shown here. The sharp feature of the unoccupied Mn d-states above E_F broadens, below E_F d states at the slope towards the Fermi energy are lost by the Si substitutions, and there appear Si-related bands more than

8 eV below E_F (not shown). The DOS at the Fermi energy depends on the Si configurations but no clear trend is observed. Both Laves phases are metallic, since there is always a small but finite DOS at E_F. This is also the case when an on-site orbital potential U_{eff} at the transition metal sites is included for the calculations.

It should be pointed out that we did not try to calculate U_{eff}, we only varied it in the range between 0 and 0.5 Ry typical for these transition metals to determine the influence on the band structure qualitatively. $U_{\text{eff}} = 0.5$ Ry is, in fact, too large, since it raises the Mn moments above 4 μ_B, which is incompatible with the value determined from neutron diffraction data. Taking the Mn moments as an indicator, $U_{\text{eff}} \approx 0.1$ was obtained, similar to the value reported for Heusler alloys.[38,39]

Note that the general behavior of the DOS is in accord with our observation of a metallic (Sommerfeld) characteristic from the low temperature specific heat (see Fig. 5) measurements for both alloys. A quantitative evaluation of the Sommerfeld constant from our band structures is, unfortunately, not possible. The systematic errors from our treatment by superlattices and from the unknown on-site correlation potential are clearly too large. Qualitatively, the calculated values for $\text{MnNi}_{1.25}\text{Si}_{0.75}$ with different Si configurations in the unit cell are at 5.0 ± 2.0 mJ/mol K^2, comparable to the experimental one (3.24 mJ/mol K^2), especially if a moderate U_{eff} is considered. However, for $\text{MnCu}_{1.65}\text{Si}_{0.35}$ we obtain consistently slightly smaller Sommerfeld constants than that for $\text{MnNi}_{1.25}\text{Si}_{0.75}$. This might be expected from the fact that the Cu d states are roughly 1 eV farther below E_F than the Ni d-states (see Fig. 14), but obviously it is in contrast to our experimental finding. Further studies are required to clarify if this is due to our approach being too simple for the band-structure calculations, or to the magnetic contributions to the low temperature specific heat masking the Sommerfeld contribution.

In the monoclinic unit cell, all four Mn sites are inequivalent. Figure 15 shows the calculated total energy E_{tot} for the three AF spin configurations discussed above (see Fig. 13) as well as for a ferromagnet (FM). All spin configurations (including nonmagnetic Mn, not shown) are local minima for the total energy in the sense that the self consistency cycle of the calculations does not change the starting spin configuration. Since the total energy strongly depends on the Si configurations, we show the difference to its minimum value E_{min} with one Si per unit cell (AF-I with the Si at one 6h site) or with two Si per unit cell (AF-IIb with two Si at the 6h sites) for unit cells with one or two Si, respectively.

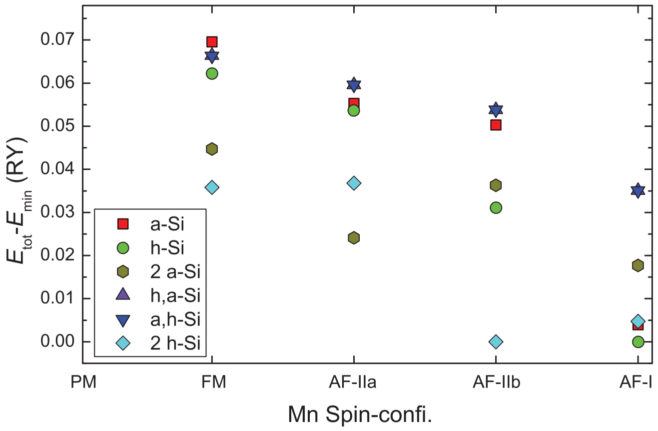

FIG. 15. (Color online) Calculated total energy of hypothetical $\text{Mn}_4\text{Cu}_7\text{Si}$ (red squares, green dots) and $\text{Mn}_4\text{Cu}_6\text{Si}_2$ (Si positions given in the figure) for Si on 2a and 6h sites and for the Mn spin configurations indicated at the horizontal axis.

The variation of the total energies with different Si configurations suggests a lower energy for Si at the 6h site; for one Si per unit cell, the energy with 6h-Si is lower for all magnetic configurations than that with 2a-Si. For two Si per unit cell, the energy depends on the Si configurations and with both Si at the 6h sites the configuration again has the lowest energy. This confirmed the site preference of Si at the 6h site observed by SCXD. The actual value of the energy difference depends, however, strongly on the configuration and cannot be related to the size of the site preference. This is not surprising since we did not attempt any structural relaxation in our calculations, nor configurations with more Si in one unit cell, nor larger supercells.

The dependence of the total energies on the magnetic configuration indicates that there is a competition between AF-IIb and AF-I being the ground state. The probability for two Si at the 6h sites is highest, favoring AF-IIb. However, the difference to the optimum AF-I for all other Si configurations is small, so AF-I should be considered to be a possible solution in the real, random structure.

Using the method described by Novak and Rusz,[40] we may estimate the exchange integrals J_1, J_2 from the calculations summarized in Fig. 15. The Heisenberg spin Hamiltonian $H_{\text{ex}} = \sum_{i \neq j} J_{ij} S_i S_j$ with exchange integrals J_{ij} coupling neighboring spins S_i, S_j results from separating the spin-dependent and the spin-independent contributions to the total energy calculated in DFT: $E_{\text{tot}} = E_{\text{ch}} + E_{\text{ex}}$. Restricting the magnetic model to Mn moments $\pm S$ of equal size with couplings J_1, J_2 between nearest and next nearest neighbors, the exchange coupling energy per Mn spin is

$$E_{\text{ex}} = J_1 S\, S + 3 J_2 S\, S. \qquad (2)$$

The relative orientation of the spins determines the sign of the two contributions. J_1 and J_2 can be determined from the difference between the calculated total energy for the AF-I and AF-IIb (for J_1) or AF-IIa (for J_2), provided that E_{ch} stays constant. The energy differences in Fig. 15 show that with only one Si per unit cell both exchange couplings are strongly antiferromagnetic ($J_1 S\, S = 600, J_2 S\, S = 350$ K for Si at one 6h site) and are lowered with two Si per unit cell ($J_1 S\, S = 370, J_2 S\ \ S = 160$ K for one Si at the 2a and 6h sites each), and have a sign change when both Si are in the layer across which the coupling occurs ($J_1 S\, S = -100, J_2 S\, S = 200$ K for AF-IIb).

The size of the calculated exchange couplings agrees reasonably well with our experimental $J \approx 70$ K for $S = 3/2$. More importantly, the strong dependence of the exchange constants on the Si configurations in the unit cell, particularly with even a change of sign for J_1, strongly supports our interpretation of the experimental low temperature data in terms of a magnetic transition. The random nature of competing positive and negative exchange couplings between temperature-dependent magnetic moments may conceivably drive an inhomogeneous phase transition between AF-IIb and AF-I, leading to the complex behavior observed in all physical properties.

We note that the data in Fig. 15 indicate certain limitations of this simple magnetic model and our way to determine its parameters. We have, in principle, more than one total energy difference to determine J_1 or J_2. However, taking the FM configuration as a reference leads to exchange couplings differing by more than a factor of two. This is attributed to the fact that DFT finds for each spin configuration a slightly different optimum electron density, leading to a different contribution E_{ch} to the total energy. Since the DOS for the three AF spin configurations is very similar, we use the values deduced with AF-I as a reference as given above.

The calculated magnetic moments located within the muffin-tin radius at Mn depend on the local Mn environment. We find moments in the range $3.7 \pm 0.2\mu_B$ in $\text{MnCu}_{2-x}\text{Si}_x$, and $3.3 \pm 0.2\mu_B$ in $\text{MnNi}_{2-x}\text{Si}_x$, both for calculations without orbital potential U, indicating $S = 3/2$ moments with an additional itinerant contribution. For Mn with Si neighbors, lower values are calculated. No significant moments were calculated for the muffin tin spheres at Cu, Ni and Si ($<0.07\mu_B$ in all cases). Considering our rather crude approximation of the random structure by periodic lattices this is in very good agreement with the moment of $2.7\mu_B$ derived from the neutron diffraction data at room temperature in $\text{MnCu}_{1.65}\text{Si}_{0.35}$ (see above). DFT calculates of course only the ground state. Our NMR results show that the sublattice magnetization at room temperature is 70% of saturation, which is $2.6 \pm 0.15\mu_B$. We note that this indicates rather small values for the orbital potential at least in $\text{MnCu}_{1.65}\text{Si}_{0.35}$ since the Mn moments increase with increasing U_{eff}. The larger Mn moments at room temperature in conjunction with the lower T_N would be compatible with a larger enhancement of the moments by U_{eff} in $\text{MnNi}_{1.25}\text{Si}_{0.75}$.

The variation of the calculated Fermi-contact hyperfine fields at Mn is much larger due to a strong influence of Si on the compensation between valence and core electron contributions. The calculated fields in $\text{MnCu}_{1.65}\text{Si}_{0.35}$ vary in the range from 3.4 to 22.0 T. We note that the corresponding frequency range for NMR zero-field resonances extends down to the frequencies where we observed weak zero field spin echos, so these signals might, in fact, be due to Mn. Unfortunately, the signal was too weak and the line was too broad to verify this by measurements of the corresponding γ in fields large enough to shift the line significantly.

If we consider only the AF-I magnetic configuration, the calculated transferred hyperfine fields at Cu fall into several groups, reflecting the periodic superstructure imposed in the calculation. Large fields (5.6 T) are predicted for the two $2a$ Cu in asymmetric configurations with one neighboring Si at one $6h$ site. This large value is a consequence of the superstructure with Si at the $6h$ sites on only one side of a given $2a$ layer. To lower fields there follows a group with fields close to 0.8, 0.5, and 0.2 T, corresponding to $6h$ Cu with a $6h$-Si neighbor, a $6h$-Si next neighbor, and $2a$-Si neighbors. The fields at the remaining Cu sites are zero within the accuracy of the calculation, reflecting Cu positions in magnetically symmetric neighborhood. In view of the interference effects expected within the real lattice with random Si distribution, these values agree reasonably well with the transferred field $B_\perp = 0.65$ T determined from the NMR spectra. The calculated transferred field at the Si nuclei is, as expected, one order of magnitude smaller (groups at 2.8 and 1.0 T in asymmetric positions, and at 0.0, ... ,0.01 T in symmetric ones), again in accord with our experimental finding in $\text{MnNi}_{1.25}\text{Si}_{0.75}$.

Finally, the calculated hyperfine fields at Cu in the AF-II magnetic configurations confirm the expectation that large transferred fields will occur in this situation. We find hyperfine fields up to 18 T at the Cu nuclei in these calculations, This is clearly more than enough to wipe out a large part of the Cu spin echo from regions where an AF-II spin arrangement exists, consistent with our explanation of the steep loss in signal intensity at low temperature (see Fig. 12).

IV. CONCLUSION

In summary, the phase relations, crystal structure, and physical properties of the MgZn_2-type Laves phases in the Mn-Cu-Si and Mn-Ni-Si systems were investigated by XSCD, XPD, ND, EPMA, transport property, magnetic susceptibility, and NMR measurements combined with band-structure calculations. Our results showed that the homogeneous regime of the Laves phase in the Mn-Cu-Si system at 800 °C ranges from 32.5 to 36.7 at.% Mn and from 11.5 to 13.5 at.% Si, significantly deviating from previous work. Accordingly, the Laves phase in the system follows the ideal stoichiometry AB_2 composition. X-ray single-crystal data combined with neutron powder diffraction clearly defined the crystal structure in both Laves phases $\text{MnCu}_{1.65}\text{Si}_{0.35}$ and $\text{MnNi}_{1.25}\text{Si}_{0.75}$: Mn atoms are preferably situated at the $4f$ site and Cu(Ni) and Si atoms share the $2a$ and $6h$ sites. Both Laves phases are antiferromagnetic with Néel temperatures $T_N \approx 800$ K for $\text{MnCu}_{1.65}\text{Si}_{0.35}$ and $T_N \approx 630$ K for $\text{MnNi}_{1.25}\text{Si}_{0.75}$, respectively. The magnetic structure derived from room temperature ND data showed that only Mn atoms at the $4f$ sites carry magnetic moments, which are aligned antiferromagnetically along the crystal c axis. The magnetic moments at room temperature are $2.7\mu_B/\text{Mn}$ for $\text{MnCu}_{1.65}\text{Si}_{0.35}$ and $2.9\mu_B/\text{Mn}$ for $\text{MnNi}_{1.25}\text{Si}_{0.75}$. These properties were confirmed by NMR measurements and DFT calculations. For $\text{MnCu}_{1.65}\text{Si}_{0.35}$ we estimate a low temperature saturation value of $3.8\mu_B/\text{Mn}$ and an exchange integral $J = 70$ K from basic spin wave theory and the NMR data. Both values are in accord with the ones predicted from DFT calculations. We provided evidence that the complex behavior of $\text{MnCu}_{1.65}\text{Si}_{0.35}$ below 100 K, which is beyond this simple model, should be assigned to a transition between two antiferromagnetic structures, driven by a Si induced distribution of exchange integrals with competing ferro- and antiferromagnetic couplings J_1 across the $6h$ sites.

ACKNOWLEDGMENTS

It is a pleasure to thank the group of K.-H. Schwarz at the TU Vienna for making Wien2k available to us. M.W.P. gratefully acknowledges financial support by the Austrian FWF under grant P21073-N20.

[*] yan@ifp.tuwien.ac.at

[†] peter.franz.rogl@univie.ac.at

[1] C. S. Smith, Trans. AIME **89**, 164 (1930).

[2] C. S. Smith and W. R. Hibbard, Trans. AIME **174**, 222 (1942).

[3] K. L. Dreyer, Metall. **7**, 186 (1953).

[4] V. D. Turkin and L. K. Kushnikova, Sb. Nauchn. Tr. Mosk. Inst. Tsvetn. Met. Zolota **29**, 18 (1958).

[5] A. P. Smiryagin and R. P. Martynyuk, Issled. Splavov Tsvet. Met., Akad. Nauk SSSR **3**, 98 (1962).

[6] W. M. Guertler, M. Guertler, and E. Anastasiadias (Jerusalem: Israel Program for Scientific Translations [available from the U.S. Dept. of Commerce, Clearinghouse for Federal Scientific and Technical Information, Springfield, Va.], 1969), USAF Contract No. AF 61(052)-74.

[7] Y. Chang and I. C. R. Association, Phase Diagrams and Thermodynamic Properties of Ternary Copper-Metal Systems, INCRA monograph (Materials Department, College of Engineering and Applied Science, University of Wisconsin-Milwaukee, 1979).

[8] N. Lebrun, in *Non-Ferrous Metal Systems. Part 2*, Landolt-Börnstein - Group IV Physical Chemistry, Vol. 11C2, edited by G. Effenberg and S. Ilyenko (Springer, Berlin, Heidelberg, 2007), pp. 332–345.

[9] K. P. Mukherjee and K. P. Gupta, Metall. Trans. **4**, 618 (1973).

[10] K. P. Mukherjee and K. P. Gupta, Trans. Indian Inst. Met. **27**, 169 (1974).

[11] J. Miettinen, Calphad **27**, 395 (2003).

[12] Y. Y. Cherkashin, Y. I. Gladyshevskiy, P. I. Kripyakevich, and Y. Kuzma, Russ. J. Inorg. Chem. **3**, 650 (1958).

[13] K. Gupta, J. Phase Equilib. Diff. **27**, 529 (2006).

[14] Y. B. Kuzma, E. I. Gladyshevskii, and E. E. Cherkashin, Russ. J. Inorg. Chem. **9**, 1028 (1964).

[15] T. Ohoyama and N. Yamada, in *Alloys and Compounds of d-Elements with Main Group Elements. Part 2*, Landolt-Börnstein - Group III Condensed Matter, Vol. 32C, edited by H. Wijn (Springer, Berlin, Heidelberg, 2001), pp. 13–38.

[16] T. Ohoyama and N. Yamada, in *Alloys and Compounds of d-Elements with Main Group Elements. Part 2*, Landolt-Börnstein - Group III Condensed Matter, Vol. 32C, edited by H. Wijn (Springer, Berlin, Heidelberg, 2001), pp. 55–59.

[17] T. Eriksson, Ph.D. thesis, Uppsala University, Sweden, 2005.

[18] M. Kolenda, A. Szytua, J. Leciejewicz, A. Pawlukoj, and H. Ptasiewicz-Bak, J. Magn. Magn. Mater. **89**, 26 (1990).

[19] M. Kolenda, A. Szytua, J. Leciejewicz, and C. Maletka, J. Magn. Magn. Mater. **96**, 121 (1991).

[20] X. Yan, X.-Q. Chen, A. Grytsiv, V. T. Witusiewicz, P. Rogl, R. Podloucky, V. Pomjakushin, and G. Giester, Int. J. Mater. Res. **4(97)**, 450 (2006).

[21] X.-L. Yan, X.-Q. Chen, A. Grytsiv, P. Rogl, R. Podloucky, H. Schmidt, G. Giester, and X.-Y. Ding, Intermetallics **16**, 16 (2008).

[22] P. Fischer, G. Frey, M. Koch, M. Konnecke, V. Pomjakushin, J. Schefer, R. Thut, N. Schlumpf, R. Burge, U. Greuter, S. Bondt, and E. Berruyer, Physica B **276-278**, 146 (2000).

[23] P. Blaha, K. Schwarz, G. Madsen, D. Kvasnicka, and J. Luitz, “WIEN2K”, http://www.wien2k.at/index.html (2011), tU-Wien.

[24] J. P. Perdew, K. Burke, and M. Ernzerhof, Phys. Rev. Lett. **77**, 3865 (1996).

[25] G. K. H. Madsen and P. Novak, Europhys. Lett. **69**, 777 (2005).

[26] V. I. Anisimov, I. V. Solovyev, M. A. Korotin, M. T. Czyżyk, and G. A. Sawatzky, Phys. Rev. B **48**, 16929 (1993).

[27] S. Blügel, H. Akai, R. Zeller, and P. H. Dederichs, Phys. Rev. B **35**, 3271 (1987).

[28] X. Yan, A. Grytsiv, P. Rogl, V. Pomjakushin, and X. Xue, J. Alloys Compd. **469**, 152 (2009).

[29] E. Parthé, L. Gelato, B. Chabot, M. Penzo, K. Cenzual, and R. Gladyshevskii, *TZPIX Standardized Data and Crystal Chemical Characterization of Inorganic Structure Types* (Springer, Berlin, 1994).

[30] A. Wills, Physica B **276-278**, 680 (2000).

[31] J. Rodríguez-Carvajal, Physica B **192**, 55 (1993).

[32] P. A. Lee and T. V. Ramakrishnan, Rev. Mod. Phys. **57**, 287 (1985).

[33] M. D. Wilding and E. W. Lee, Proc. Phys. Soc. **65**, 955 (1965).

[34] T. Oguchi, Phys. Rev. **117**, 117 (1960).

[35] F. B. Anderson and H. B. Callen, Phys. Rev. **136**, A1068 (1964).

[36] F. Keffer, in *Encyclopedia of Physics*, edited by S. Flügge and H. P. J. Wijn (Springer, Berlin, 1966), Vol. 18.2.

[37] E. A. Turov and M. P. Petrov, *Nuclear Magnetic Resonance in Ferro- and Antiferromagnets* (Wiley, New York, 1972).

[38] B. Balke, G. H. Fecher, H. C. Kandpal, C. Felser, K. Kobayashi, E. Ikenaga, J.-J. Kim, and S. Ueda, Phys. Rev. B **74**, 104405 (2006).

[39] J. Winterlik, G. H. Fecher, B. Balke, T. Graf, V. Alijani, V. Ksenofontov, C. A. Jenkins, O. Meshcheriakova, C. Felser, G. Liu, S. Ueda, K. Kobayashi, T. Nakamura, and M. Wójcik, Phys. Rev. B **83**, 174448 (2011).

[40] P. Novák and J. Rusz, Phys. Rev. B **71**, 184433 (2005).